

Nanopillar templating of biopolymer hydrogels augments stiffness and strength

Sara Heedy (✉ sheedy@uci.edu)

University of California Irvine <https://orcid.org/0000-0001-7763-0447>

Juviarelli Pineda

University of California Irvine

Albert Yee

University of California Irvine

Article

Keywords: biopolymers, nanoscience, structural tissue

Posted Date: June 4th, 2021

DOI: <https://doi.org/10.21203/rs.3.rs-583918/v1>

License: © ⓘ This work is licensed under a Creative Commons Attribution 4.0 International License.

[Read Full License](#)

Abstract

In nature, structural biopolymers are highly organized to allow for the development of complex tissues within a living entity, including the human body. To match the properties found in these fibrous structural tissues, synthetic biomimetic hydrogels must have an optimal combination of stiffness, strength, and toughness; though an ideal combination remains challenging to achieve. Here, we report a general strategy to design stiff, strong, and tough hydrogels by confining biopolymers with a balance of rigid and weak domains into nanopillar topography. The confinement within nanopillars templates the fiber assembly process throughout the bulk of the film. Compared to a flat control, the application of the nanopillar topography increases the bulk stiffness $\sim 160\%$ to 20 MPa, strength $\sim 350\%$ to 36 MPa, and toughness $\sim 450\%$ to $8,500 \text{ kJ m}^{-3}$. This simple templating strategy is suitable for a vast range of hydrogels, opening up the potential applications for a diverse array of materials.

Introduction

Naturally occurring tissues, such as skin and cartilage, have robust mechanical properties which are obtained via the assembly of fibrous building blocks into larger structures. These structures have outstanding and unusual mechanical properties due to the hierarchical variation of orientation and concentration¹⁻³. The fibrillar structures are rich in both strongly and weakly bonded domains that allow for re-organization and adaptation with an applied load⁴. Synthetic hydrogels can closely mimic biological tissues due to the copious amounts of water within the matrix. However, historically synthetic hydrogels have been considered weak, and not suitable for structural applications such as in tissues⁵. There has been significant interest in the development of stiff, strong and tough biomimetic hydrogels for applications in artificial tissues such as cartilage and skin^{6,7}.

Strategies to obtain strong and tough hydrogels include the use of double-network hydrogels, noncovalent interactions, and applying orientation to the network. A few of the first strong and tough structural hydrogels were double-network hydrogels consisting of a tightly crosslinked rigid and brittle network and a loosely crosslinked soft and ductile network⁸. The rigid and brittle hydrogel network acts as sacrificial bonds to dissipate energy by breaking into small clusters upon crack propagation. The sacrificial bonds are critical for dissipating energy and achieving the high toughness characteristic of the double-network gels⁹. Noncovalent interactions, such as ionic¹⁰ and hydrogen bonding^{11,12} (H-bonding) can lead to increased strength and stiffness. When multiple bonds are clustered together, the bonds act cooperatively and break concurrently, therefore stabilizing and strengthening the material^{13,14}. Imparting orientation through the physical confinement of constituents during fabrication can control tensile stiffness, strength, and toughness¹⁵⁻¹⁷.

Embossing and imprinting techniques have been used for millennia, an early demonstration of this is Egyptians molding with clay. Thousands of years later, this technique has been developed into a quick and straightforward method to replicate features from the macro into the nanoscale onto a polymer

surface^{18,19}. When the dimension of the replicated pattern approaches the scale of the polymer chain, the polymer molecule is confined within the pattern²⁰. The flow of the polymer chain into the cavity causes viscous flow and chain orientation due to the nanoscale dimension, and dimensional reduction during shear^{21,22}. Polymers tend to align along flow lines during deformation, subsequently the lithography process induces long range polymer alignment^{23,24}.

Herein, we demonstrate a new approach to modulating the mechanical response of fibrous linear biopolymer hydrogels and films through the application of a confining physical surface topography. The free-standing films with nanopillars are generated by dropcasting the biopolymer solutions onto a mold with nanohole topography, subsequently the polymer solution infiltrates the nanoholes and forms nanopillars. We demonstrate that the polymer chain alignment induced by nanohole infiltration increases the clustered, rigid bonds and ordered domains. The domain formation causes a cascading effect that increases the inter- and intra-chain interactions in regions far from the nanostructure interface, subsequently templating the fibrillar assembly throughout the material. The strong, clustered bonds serve to strengthen the matrix of weak, reversible bonds, analogous to the toughening mechanism in double-network hydrogels²⁵. Through the design of our materials, we introduce the use of surface topography for confining nanofibrils into knots that enhance stiffness, strength, and toughness.

Nanopillar Topography Templates The Nanofiber Assembly

Chitosan, alginate, cellulose, and chitin are all hydrogen bonding, fiber-forming biopolymers. Chitin is an abundant linear polysaccharide found in the structural skeleton in crustacean and fungal walls²⁶. The transformation of the C-2 acetamide groups in chitin into primary amino groups results in chitosan, although the deacetylation is rarely complete²⁷. A high degree of deacetylation in chitosan renders it soluble in weak acids²⁸. Here, we dissolved chitosan powder in 0.1 M acetic acid. SEM imaging reveals the aggregation of chitosan building blocks into nanofibrils approximately 58 nm in diameter and up to the micrometer range in length (Fig. 1-b, Supplementary Fig. 1). The nanofibrils bundle to form fibers ~ 1 μm in diameter (Fig. 1-c).

The free-standing films were fabricated by drop-casting the polymer solutions onto molds (additional details in Supplementary information). The solvent was evaporated overnight, creating water-soluble chitosan films. The films are rendered water insoluble by neutralizing them in a 10 wt.% sodium hydroxide solution²⁹. The neutralization prevents ionic repulsion between the chains, allowing the formation of weak reversible H-bonds, rigid H-bond clusters, and crystallites between the fibrous chitosan chains³⁰ (Fig. 1-d). The films are dried, then peeled from the mold.

Films with nanopillar topography were made in a similar fashion (Fig. 1-a). We used molds with nanohole periodicities 200 nm, 300 nm and 500 nm, referenced here as P200, P300 and P500 (Supplementary Table 1). The nanohole dimensions are comparable to but larger than the characteristic nanofibril size of chitosan^{20,31}. These length scales ensured that the fibrils were confined within the nanopillar topography

if they were able to infiltrate the nanoholes during the drop casting process. The fibril polymer chains are aligned during infiltration via extensional flow at the nanohole entrance and high shear stress at the nanohole wall³². The fibrils consequently bundle into fibers. The aligned fibrils in the fibers form rigid bond clusters and ordered domains that enhance the fiber alignment and interactions throughout the bulk of the film. As the solvent is evaporated, the fiber chain alignment is preserved³³. The fibrous network throughout the bulk film is therefore anchored by the orientation and alignment at the surface layer (Fig. 1-e).

SEM images of the films (Fig. 1-f) confirm good replication of the nanopillar arrays across the entire sample surface. The P200 film nanopillars, however, collapsed into hierarchical clusters (Fig. 1-f), while the P300 and P500 film show stable nanopillars without clustering or bunching. We confirmed the nanoscale morphology of the films formed by this process by freeze-drying them and examining them with AFM (Supplementary Fig. 2). The root mean square roughness (rms) of the flat film is 12.4 nm, increasing to 72.5 nm in the P300 film.

Mechanical Response Of Templated Nanopillar Films

We characterized the mechanical properties of the fibrous films in uniaxial tension. The films were trimmed into rectangular film specimens with a gauge length (between grips) of 10 mm and width of 2 mm, such that the nanopillars were perpendicular to the plane of the film (Fig. 2-a, Supplementary Fig. 3). The tensile tests were performed at a strain rate of 0.3 mm min^{-1} . A flat hydrogel film at equilibrium swelling was used as a control. The typical stress-strain curve of the control is shown by the blue curve in Fig. 2-b. The mechanical properties are typical of neutralized chitosan films (Supplementary Table 2).

The size of the nanopillars significantly enhanced the macroscopic mechanical response, following the order: P500 > P300 > P200 > Flat (Fig. 2-c, Supplementary Fig. 4). The slope in the initial region of the stress-strain curve, which represents the Young's modulus E of the film, is strongly affected by increasing the nanopillar dimensions (Fig. 2-d, Supplementary Table 3). The greatest increase in E was observed in the P500 film, with $E \sim 20.7 \text{ MPa}$, a $\sim 160\%$ increase relative to the control. The enhanced modulus is driven by a high total number of crosslinks (both weak and rigid). Thus, simply by adding the surface topography, the modulus of the material became comparable to that of skin (Fig. 2-j, Supplementary Table 4).

The slope of the stress-strain curve after the proportionality limit, the tangent modulus E_{tangent} , increased to 89.7 MPa in the P500 film, a $\sim 170\%$ increase relative to the control (Fig. 2-e). Additionally, the toughness of the P500 film, defined here as the work at break, increased significantly to 8.5 MJ m^{-3} , a $\sim 450\%$ increase (Fig. 2-f). The high toughness observed is consistent with the existence of large, rigid sacrificial domains within the nanopillar topography films (Fig. 2-h). The stress at break σ_b increased to 36.8 MPa, a $\sim 350\%$ increase in strength compared to the control (Fig. 2-g). The high strength of the film is attributed to the large number of rigid H-bond clusters. The strength surpasses other high-strength

Loading [MathJax]/jax/output/CommonHTML/jax.js Supplementary Table 5).

While the stiffness, strength, and toughness increased the most with the P500 film, the maximum strain, ϵ_{max} of the films was unique in that the P300 film had the greatest fracture strain of $\sim 80\%$, compared to 50% in the flat film (Supplementary Fig. 4). The fracture strains decreased in the order $P300 > P200 \sim P500 > \text{flat}$. The smaller P300 size results in a less highly aligned fibrous network, and fewer sacrificial, rigid H-bond clusters. The fibers within the P500 topography are more highly aligned within the cavity – perhaps due to the greater hole depth. Consequently, the converging fibrous network is more highly aligned within the P500 film, leading to a denser network of rigid bonds, and the film is unable to stretch as much as the P300 film. The situation is analogous to flow convergence just before the entrance region in a spinneret³⁴.

Origin Of Process-structure-property Relationship

The periodicity P_s of the nanopillars in our strained samples was determined by application of two-dimensional fast Fourier Transform (2D FFT) to the AFM images (Fig. 3-b). The periodicity of the unstrained sample, $P_o = P_s (\epsilon=0)$, was calculated to be 460 nm and 205 nm for the P500 and P300 samples, respectively. P_o slightly decreased in comparison to the corresponding freeze-dried sample, probably due to the loss of some water from the films. In both the P300 and P500 samples, the periodicity increased exponentially with the application of strain, $P_s(\epsilon) = P_o \exp(\epsilon r - 1)$, similar to the non-linear stress-strain behavior observed in the tensile experiments (Fig. 3-c).

The aspect ratio ($\eta = h d^{-1}$) of the P500 film decreased from 1.7 to 1.2 (Fig. 3-d, Supplementary Fig. 5, Supplementary Table 6). On the other hand, that of the P300 film was largely independent of the applied tensile strain. The difference may indicate that there is a threshold that must be met for the nanopillars to deform during tensile deformation. This may be related to the diameter of the cavity, which must be wide enough to accommodate multiple nanofibrils to form bundles. Our results suggest that the fiber bundles pulled out during loading in the P500 film, but not in the P300 film.

Inter-chain And Inter-layer Microstructural Organization

We sought to understand the influence of nanopillars on the bulk film composition and microstructure. The water content of the hydrated films remained at $60\text{--}70\%$, similar to that in naturally occurring cartilage (Supplementary Table 3)³⁵. Even before hydration, in the as-prepared state, the modulus E increased to 2.2 GPa in the P500 film, a $\sim 57\%$ increase compared to the control (Supplementary Fig. 6, Supplementary Table 7). This result indicates that rigid, sacrificial bonds had formed during the fabrication procedure, prior to the introduction of water.

We confirmed that the as-prepared P500 and flat films contained different quantities of rigid bonds with loading-unloading tests. Both the flat and P500 films demonstrated mechanical hysteresis, indicating the existence of rigid, sacrificial bonds and weak, reversible bonds within the films (Fig. 4-a). The P500 film exhibited a large hysteresis, which is consistent with the fracture of rigid, sacrificial clusters and bonds³⁶

Loading [MathJax]/jax/output/CommonHTML/jax.js er bonds are able to recover and reform within both the flat

and P500 films. The greater portion of fractured sacrificial bonds within the P500 film are unable to completely recover and reform, consistent with the greater hysteresis area in the P500 film compared to the flat film (Fig. 4-b). The results show that the flat film contains weak, reversible bonds.

In the as-prepared dry state the film thicknesses are $\sim 20 \mu\text{m}$ (Fig. 4-c). At equilibrium swelling, the thickness of the flat films increased 144%, while the thickness of the films with P500 topography increased by only 45%. The restriction of polymer chains during fabrication causes a denser, more ordered matrix³⁷. X-ray diffraction results confirm that both the as-prepared nanopillar and control films contain crystalline domains between random amorphous coils (Fig. 4-f, Supplementary Table 8). The more prominent diffraction peaks in the P500 films indicate that they have a larger number of crystalline domains than the control film. The strong attractive effect of the H-bonding results in the large number of crystalline domains. This is consistent with the existence of rigid, sacrificial bonds.

Generality Of Nanopillar Templating Strategy

Our templating strategy confines polymer chains within nanopillar topography enhancing the formation of rigid, sacrificial bonds within a weakly bonded network. We chose to contrast the rigid, sacrificial bonds against weak, reversible bonds by crosslinking chitosan films with either the chemical crosslinker genipin, or the physical crosslinker tripolyphosphate (TPP). The chemical crosslinks should act as rigid bonds within the network and enhance the mechanical properties (Fig. 5-a). The physical crosslinks should act as weak, reversible bonds within the network and should not enhance the mechanical properties (Fig. 5-b). We chose to utilize only the P300 and P500 surfaces, as we expect that the most significant mechanical improvement will occur with these larger surface structures.

We chemically crosslinked the chitosan films with genipin, a common crosslinker for amine-containing biomaterials^{38,39}. The genipin crosslinked chitosan system displays hierarchical fiber assembly (Supplementary Fig. 7). Uniaxial tensile testing verified that the nanopillar topography enhanced the mechanical properties of the material (Fig. 5-c). The control film has a Young's modulus E of 3.8 MPa. The E increased to 13.1 MPa for the P500 film, a $\sim 245\%$ increase compared to the control. The enhanced E in the nanopillared films confirms that a greater quantity of rigid crosslinks and interactions formed in comparison to the control. However, these permanent, rigid crosslinks are unable to reform after fracture, resulting in a low ϵ_{max} . These results illustrate that permanent crosslinks networks confined into nanopillar topography form rigid bond clusters that tune the mechanical properties.

Next, we examined chitosan films crosslinked with the physical crosslinker TPP, which forms weak, reversible bonds. The ionically TPP crosslinked network lacks rigid, sacrificial components. The TPP crosslinked control film had a E of ~ 1.3 MPa, much less than the chemically crosslinked film, an expected result due to the dynamic nature of ionic bonds³⁰. The TPP crosslinked films with nanopillar topography had a similar E to the control film (Fig. 5-d). This is due to the dynamic, reversible bonds in the ionic network which can quickly reform after deformation. These results illustrate that a balance of

Loading [MathJax]/jax/output/CommonHTML/jax.js enhance the mechanical properties via nanopillar templating.

We demonstrate the generality of our templating strategy by applying nanopillar surface topography onto films cast from the biopolymer alginate. The alginate film is ionically crosslinked with the divalent cation of calcium (Ca^{2+}) to form a Ca-alginate hydrogel. Unlike the chitosan films which contain rigid H-bond clusters and weak, reversible H-bonds, the Ca-alginate hydrogel contains both hydrogen and weak, sacrificial ionic bonds⁴⁰. The H-bonds should only be rigid prior to hydration, when there is no water to compete with them.

We confirmed that nanopillars were replicated onto the Ca-alginate surface (Supplementary Fig. 8). We found an increase in the number of crystalline domains in the as-prepared Ca-alginate film when imprinted with a nanopillar surface (Supplementary Fig. 9), consistent with the hypothesis that the interchain interaction in the nanopillared films was enhanced. We began to characterize the mechanical properties of the dry, as-prepared Ca-alginate films. The mechanical tests show that E increased $\sim 38\%$ from 2.6 GPa in the flat film to 3.6 GPa in the P500 film, respectively (Supplementary Fig. 10). This confirms the nanopillared ca-alginate film contains a greater quantity of crosslinks. After 24 hours immersed in water, the nanopillar surface relaxed into the bulk as the ionic crosslinks dynamically broke and reformed⁴¹, therefore disrupting the balance of strong and weak bonds. As a result, the mechanical properties of the hydrated film are independent of surface topography.

Discussion

In summary, we demonstrate that confinement within nanopillar topography templates the fiber assembly process of fibrous biopolymers and represents a general strategy to design stiff, strong and tough hydrogels. The biopolymer flow into the nanohole during fabrication facilitates the confinement and close packing of its chains which causes a cascading effect of enhanced rigid, sacrificial domains throughout the bulk film. To the authors' knowledge, the previous free standing polymer films that feature nanostructure topography have demonstrated a decrease in the mechanical properties compared to a flat control^{42,43}. These nanopillared hydrogels are the first example to demonstrate that surface topography can make a hydrogel stiff and strong. As revealed in the present study, a requirement for this templating strategy is the existence of both rigid, sacrificial domains and weak bonds. In short, this nanopillar templating method presents a unique strategy to achieve high stiffness, strength, and toughness in biopolymer films.

Considering that strong interactions are present in many forms, such as hydrogen bonds, covalent bonds, and crystalline domains, we foresee this templating method will not be restricted to the systems presented here. We envision that this relationship could be extended to other length scales in which strengthening and stiffening behavior is desirable. If our conclusion is correct, then the structural surface pattern only needs to be larger than the typical density fluctuation in a material. This generalized templating strategy is suitable for a vast range of originally weak hydrogels, opening up the range of possible materials for a diverse range of applications.

Declarations

Acknowledgements

The authors thank the laboratory of Prof. Alon Gorodetsky for access to the freeze-dryer. The authors acknowledge the use of facilities and instrumentation at the UC Irvine Materials Research Institute (IMRI), which is supported in part by the National Science Foundation through the UC Irvine Materials Research Science and Engineering Center (DMR-2011967). AFM work was performed using an Anton Paar Tosca 400 AFM on loan to IMRI from Anton Paar GmbH. This work was supported by the Department of Defense (DoD) Peer-Reviewed Medical Research Program (PRMRP) award no. W81XWH-17-0355.

Author contributions

S.H. conceived the concept. A.F.Y. supervised the project and discussed the results. S.H. conducted the experiments. J.P. helped with fabrication. S.H. and A.F.Y. wrote the manuscript, and all of the authors provided feedback.

Methods

Methods are available in the Supplementary Information.

References

1. Meyers, M. A., McKittrick, J. & Chen, P.-Y. Structural Biological Materials: Critical Mechanics-Materials Connections. *Science***339**, 773–779 (2013).
2. Kong, W. *et al.* Muscle-Inspired Highly Anisotropic, Strong, Ion-Conductive Hydrogels. *Adv. Mater.***30**, 1801934 (2018).
3. Zou, J. *et al.* Highly Efficient and Environmentally Friendly Fabrication of Robust, Programmable, and Biocompatible Anisotropic, All-Cellulose, Wrinkle-Patterned Hydrogels for Cell Alignment. *Adv. Mater.***31**, 1904762 (2019).
4. Ling, S., Kaplan, D. L. & Buehler, M. J. Nanofibrils in nature and materials engineering. *Nat. Rev. Mater.***3**, 18016 (2018).
5. Calvert, P. Hydrogels for soft machines. *Adv. Mater.***21**, 743–756 (2009).
6. Hua, M. *et al.* Strong tough hydrogels via the synergy of freeze-casting and salting out. *Nature***590**, 594–599 (2021).
7. Prince, E. & Kumacheva, E. Design and applications of man-made biomimetic fibrillar hydrogels. *Nat. Rev. Mater.***4**, 99–115 (2019).
8. Gong, J. P., Katsuyama, Y., Kurokawa, T. & Osada, Y. Double-Network Hydrogels with Extremely High Mechanical Strength. *Adv. Mater.***15**, 1155–1158 (2003).
9. Chen, Q., Chen, H., Zhu, L. & Zheng, J. Fundamentals of double network hydrogels. *J. Mater. Chem.*

10. Sun, T. L. *et al.* Physical hydrogels composed of polyampholytes demonstrate high toughness and viscoelasticity. *Nat. Mater.***12**, 932–937 (2013).
11. Hu, X., Vatankhah-Varnoosfaderani, M., Zhou, J., Li, Q. & Sheiko, S. S. Weak Hydrogen Bonding Enables Hard, Strong, Tough, and Elastic Hydrogels. *Adv. Mater.***27**, 6899–6905 (2015).
12. Song, P. & Wang, H. High-Performance Polymeric Materials through Hydrogen-Bond Cross-Linking. *Adv. Mater.***32**, 1–12 (2020).
13. Li, J. *et al.* Observation of α -Helical Hydrogen-Bond Cooperativity in an Intact Protein. *J. Am. Chem. Soc.***138**, 1824–1827 (2016).
14. Giesa, T., Pugno, N. M., Wong, J. Y., Kaplan, D. L. & Buehler, M. J. What's inside the box? - Length-scales that govern fracture processes of polymer fibers. *Adv. Mater.***26**, 412–417 (2014).
15. Isaacson, S. G. *et al.* Fundamental limits of material toughening in molecularly confined polymers. *Nat. Mater.***15**, 294–298 (2016).
16. Keten, S., Xu, Z., Ihle, B. & Buehler, M. J. Nanoconfinement controls stiffness, strength and mechanical toughness of β -sheet crystals in silk. *Nat. Mater.***9**, 359–367 (2010).
17. Mredha, M. T. I. *et al.* A Facile Method to Fabricate Anisotropic Hydrogels with Perfectly Aligned Hierarchical Fibrous Structures. *Adv. Mater.***30**, 1–8 (2018).
18. Chou, S. Y., Krauss, P. R. & Renstrom, P. J. Imprint of sub-25 nm vias and trenches in polymers. *Appl. Phys. Lett.***67**, 3114 (1995).
19. Chou, S. Y., Krauss, P. R. & Renstrom, P. J. Nanoimprint lithography. *J. Vac. Sci. Technol. B Microelectron. Nanometer Struct.***14**, 4129–4133 (1996).
20. Pierre-Gilles de Gennes. *Scaling Concepts in Polymer Physics*. (Cornell University Press, 1979).
21. Rowland, H. D., King, W. P., Pethica, J. B. & Cross, G. L. W. Molecular Confinement Accelerates Deformation of Entangled Polymers During Squeeze Flow. *Science* **720–724** (2008).
22. Teisseire, J., Revaux, A., Foresti, M. & Barthel, E. Confinement and flow dynamics in thin polymer films for nanoimprint lithography. *Appl. Phys. Lett.***98**, 1–4 (2011).
23. Hu, Z. & Jonas, A. M. Control of crystal orientation in soft nanostructures by nanoimprint lithography. *Soft Matter***6**, 21–28 (2009).
24. Wang, J., Sun, X., Chen, L., Zhuang, L. & Chou, S. Y. Molecular alignment in submicron patterned polymer matrix using nanoimprint lithography. *Appl. Phys. Lett.***77**, 166–168 (2000).
25. Haque, Md. A., Kurokawa, T. & Gong, J. P. Super tough double network hydrogels and their application as biomaterials. *Polymer***53**, 1805–1822 (2012).
26. Jang, M. K., Kong, B. G., Jeong, Y. I., Lee, C. H. & Nah, J. W. Physicochemical characterization of α -chitin, β -chitin, and γ -chitin separated from natural resources. *J. Polym. Sci. Part Polym. Chem.* (2004) doi:10.1002/pola.20176.
27. Islam, S. Chitin and Chitosan: Structure, Properties and Applications in Biomedical Engineering. *J Polym Env.* **13** (2017).

28. Pillai, C. K. S., Paul, W. & Sharma, C. P. Chitin and chitosan polymers: Chemistry, solubility and fiber formation. *Prog. Polym. Sci. Oxf.***34**, 641–678 (2009).
29. Bhattarai, N., Gunn, J. & Zhang, M. Chitosan-based hydrogels for controlled, localized drug delivery. *Adv. Drug Deliv. Rev.***62**, 83–99 (2010).
30. Berger, J. *et al.* Structure and interactions in covalently and ionically crosslinked chitosan hydrogels for biomedical applications. *Eur. J. Pharm. Biopharm.***57**, 19–34 (2004).
31. Giesa, T. & Buehler, M. J. Nanoconfinement and the Strength of Biopolymers. *Annu. Rev. Biophys.***42**, 651–673 (2013).
32. Becraft, M. L. & Metzner, A. B. The rheology, fiber orientation, and processing behavior of fiber-filled fluids. *J. Rheol.***36**, 143–174 (1992).
33. Kawada, J., Abe, Y., Yui, T., Okuyama, K. & Ogawa, K. Crystalline Transformation of Chitosan from Hydrated to Anhydrous Polymorph Via Chitosan Monocarboxylic Acid Salts. *J. Carbohydr. Chem.***18**, 559–571 (1999).
34. Xia, X., Wang, J., Wang, H. & Zhang, Y. Numerical investigation of spinneret geometric effect on spinning dynamics of dry-jet wet-spinning of cellulose/[BMIM]Cl solution. *J. Appl. Polym. Sci.***133**, (2016).
35. Sophia Fox, A. J., Bedi, A. & Rodeo, S. A. The Basic Science of Articular Cartilage: Structure, Composition, and Function. *Sports Health Multidiscip. Approach***1**, 461–468 (2009).
36. Gong, J. P. Why are double network hydrogels so tough? *Soft Matter***6**, 2583 (2010).
37. Martinez, A. W., Caves, J. M., Ravi, S., Li, W. & Chaikof, E. L. Effects of crosslinking on the mechanical properties, drug release and cytocompatibility of protein polymers. *Acta Biomater.***10**, 26–33 (2014).
38. Heedy, S., Marshall, M., Pineda, J. J., Pearlman, E. & Yee, A. F. Synergistic Antimicrobial Activity of a Nanopillar Surface on a Chitosan Hydrogel. *ACS Appl. Bio Mater.***3**, 8040–8048 (2020).
39. Sung, H. W., Huang, R. N., Huang, L. H. & Tsai, C. C. In vitro evaluation of cytotoxicity of a naturally occurring cross-linking reagent for biological tissue fixation. *J. Biomater. Sci. Polym. Ed.***10**, 63–78 (1999).
40. Braccini, I. & Pérez, S. Molecular Basis of Ca²⁺-Induced Gelation in Alginates and Pectins: The Egg-Box Model Revisited. *Biomacromolecules***2**, 1089–1096 (2001).
41. Zhao, X., Huebsch, N., Mooney, D. J. & Suo, Z. Stress-relaxation behavior in gels with ionic and covalent crosslinks. *J. Appl. Phys.***107**, 063509 (2010).
42. Greiner, C. Adhesion of Bioinspired Micropatterned Surfaces: Effects of Pillar Radius, Aspect Ratio, and Preload. 8.
43. Wang, X., Tan, D., Zhang, X., Lei, Y. & Xue, L. Effective Elastic Modulus of Structured Adhesives: From Biology to Biomimetics. *Biomimetics***2**, 10 (2017).

Figures

Loading [MathJax]/jax/output/CommonHTML/jax.js

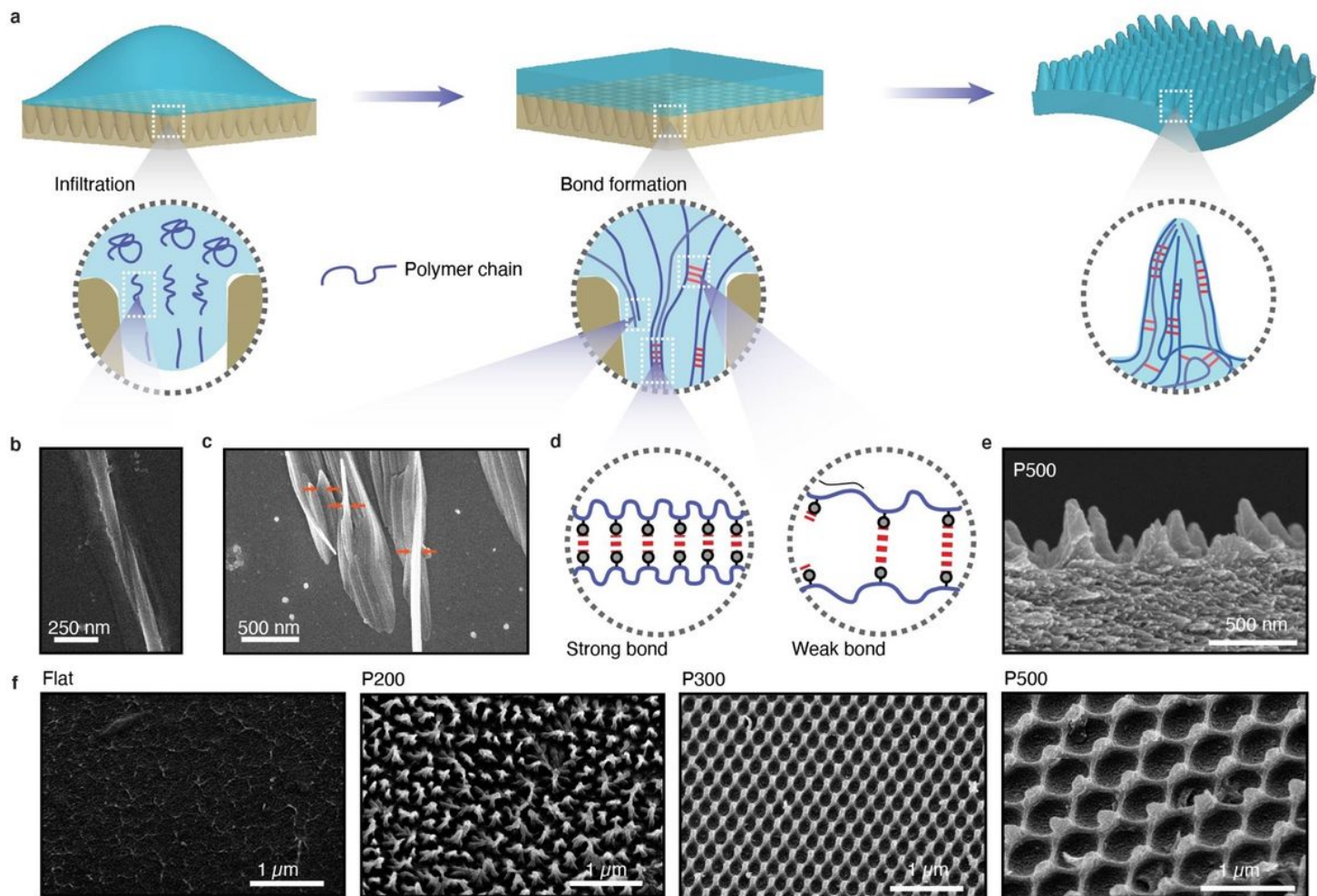


Figure 1

Integration of the nanopillar surface structure that templates the fiber assembly in the hydrogel films (a) An illustration of the nanopillar fabrication process. The polymer solution is dropcast onto the nanohole mold, and the polymer chains infiltrate the mold nanocavities. As the solvent is evaporated the chitosan chains bundle together into fibers with strong and weak bonds that stabilize the structure. The nanopillars enhance the formation of strong bonds. A free-standing polymer film is peeled from the mold. (b) A twisted chitosan fibril. (c) Chitosan fibrils assemble hierarchically into fibers $\sim 1 \mu\text{m}$ in diameter. (d) An illustration of the bonds of present within the network. The rigid bonds serve as sacrificial bonds that break during deformation. (e) SEM micrograph of the P500 fracture surface. The fibers infiltrated the nanopillars and demonstrate the internal morphology of the structures. (f) Representative SEM of the hydrated film surfaces after freeze drying. The flat control film shows a fibrous, porous surface. The nanopillar films have a periodic surface texture. The P200 film nanopillars collapsed and bundled together, while the P300 and P500 film nanopillars are stable without bundling. SEM micrographs were taken at a 30° tilt.

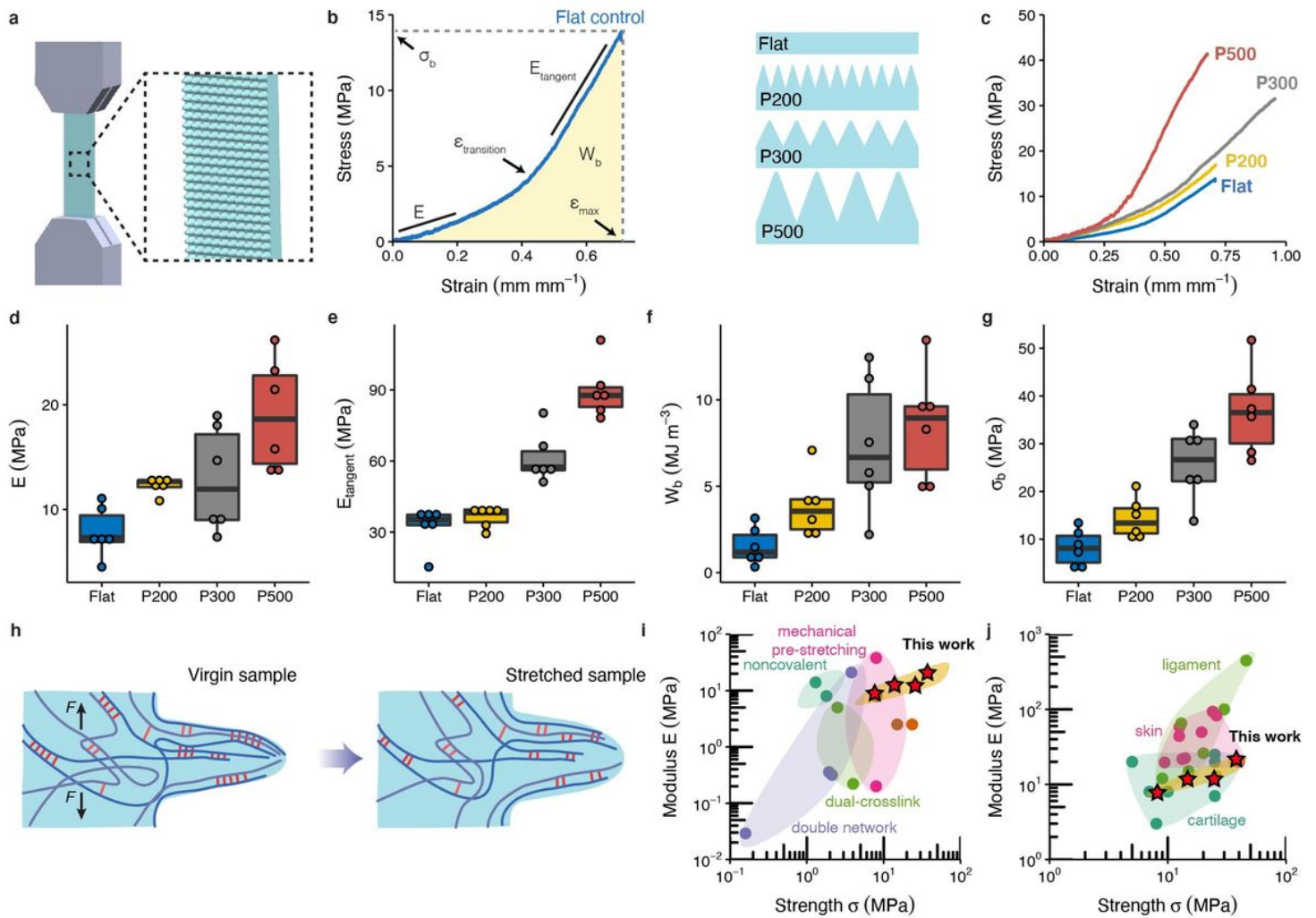


Figure 2

Nanopillars on a fibrous biopolymer film enhance the bulk mechanical properties. (a) Schematic of the in-plane tensile testing set-up, demonstrating the nanopillar direction relative to the tensile stress. (b) Typical stress-strain curve of the flat hydrogel film at equilibrium swelling. The slope of the initial linear region defines the Young's modulus, E . This region is followed by a transition strain, $\epsilon_{\text{transition}}$, after which the slope of the second linear region defines the tangent modulus, E_{tangent} . Finally, failure occurred at the maximum stress, which defines the stress at break σ_b and the maximum strain, ϵ_{max} . The area under the stress-strain curve is the work at break, W_b . (c) Typical stress-strain curves of the hydrogels that demonstrate the increase in stiffness and strength with the addition of the nanopillar topography. (d-g) Dependence of the modulus (d), tangent modulus (e), work at break (f), and the stress at break (g) of the templated hydrogels. (h) Illustration of a single nanopillar under uniaxial mechanical deformation. The rigid bonds that formed during infiltration into the nanopillar sacrificially fracture resulting in the high stiffness, strength, and toughness of the material. (i) Ashby diagrams of the modulus versus strength of our templated hydrogel (stars) and other reported strong and stiff hydrogels. (j) Ashby diagram of the modulus versus strength of our templated hydrogels and tissues (stars). The data used is summarized in [Supplementary Table 4](#) and [5](#). Mechanical data are from $n=6$ films.

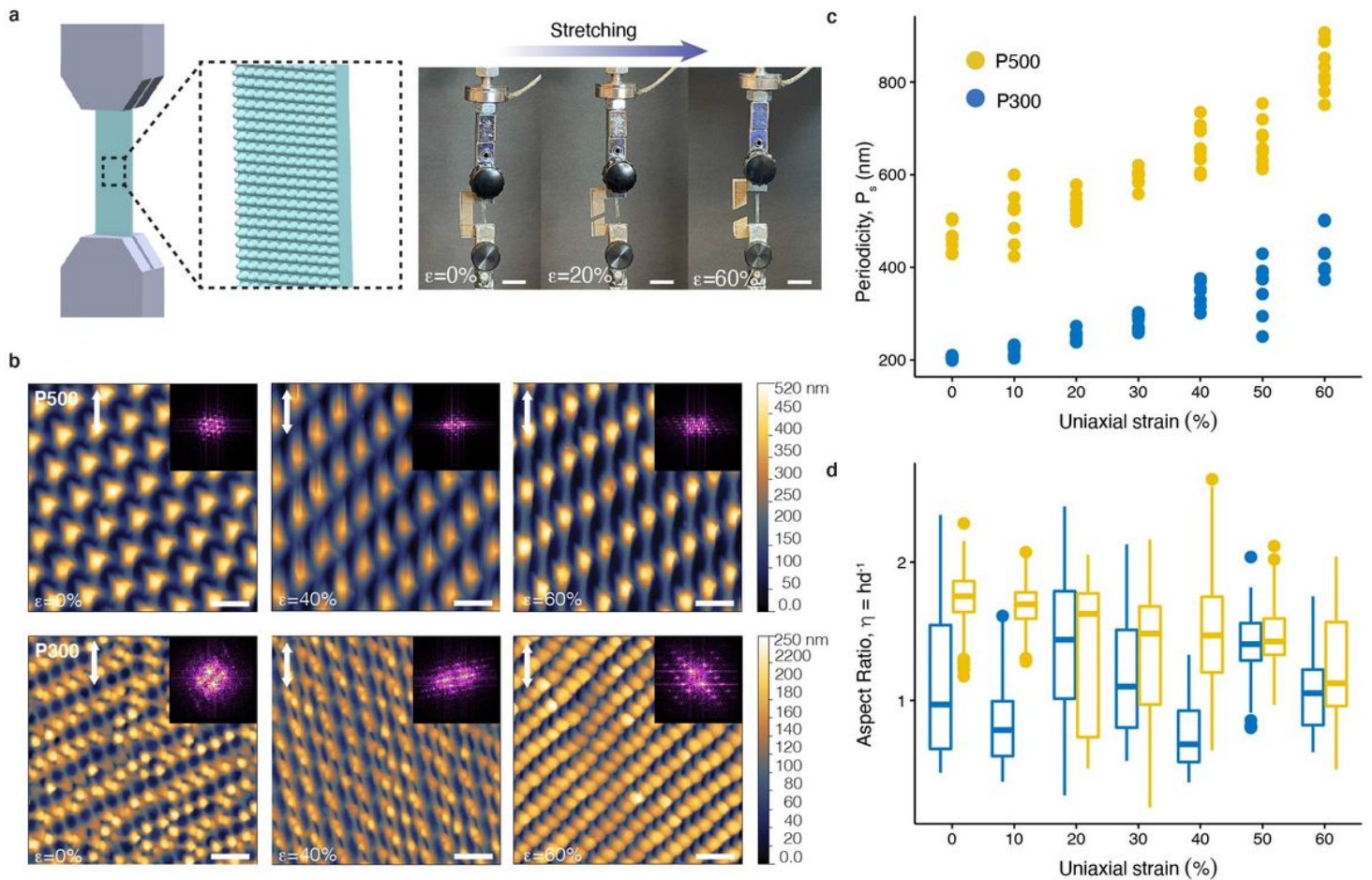


Figure 3

Morphology of the mechanically strained nanopillar hydrogel films. (a) Schematic and photographs of nanopillar films under tensile strain. Scale bars are 1 cm. (b) AFM micrographs of the P500 and P300 films corresponding to the unstrained ($\epsilon=0\%$), $\epsilon=40\%$, and $\epsilon=60\%$ samples. Insets are the corresponding 2D FFT images. (c) The dependence of the periodicity, P_s , on uniaxial tensile strain. The periodicity was calculated through 2D FFT analysis of the images. (d) The dependence of the aspect ratio, $\eta = h d^{-1}$, on the uniaxial tensile strain. The AFM strain analysis was performed on 3 regions in 3 films, for a total of 9 regions each. Scale bars are 500 nm.

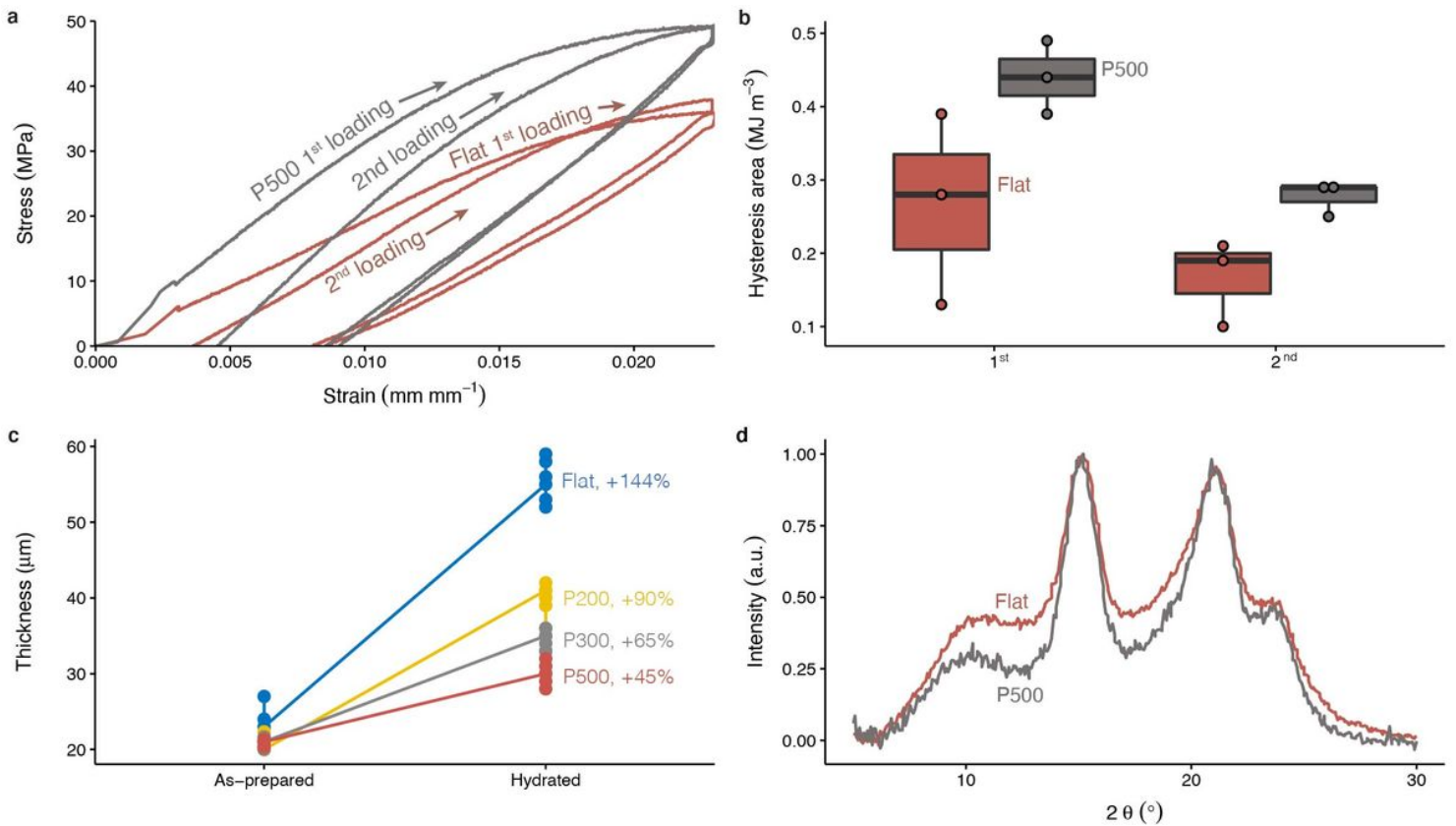


Figure 4

Condensed long-range order of the nanopillar films. (a) Recovery of the control and nanopillared film after loading-unloading tensile tests. (b) Hysteresis area after the first and second loading-unloading cycle for the flat and nanopillar films. (c) Dependence of the film thickness on the nanopillar topography in the as-prepared state and after hydration in water for 24 hours. The P500 film exhibits the smallest thickness change. (d) XRD of the as-prepared flat and P500 films. The flat film has a larger amorphous domain and broader crystalline peaks compared to the P500 film which has more prominent peaks. For comparison, the composite XRD intensity of the two films are normalized with respect to the maxima at $2\theta \sim 15^\circ$.

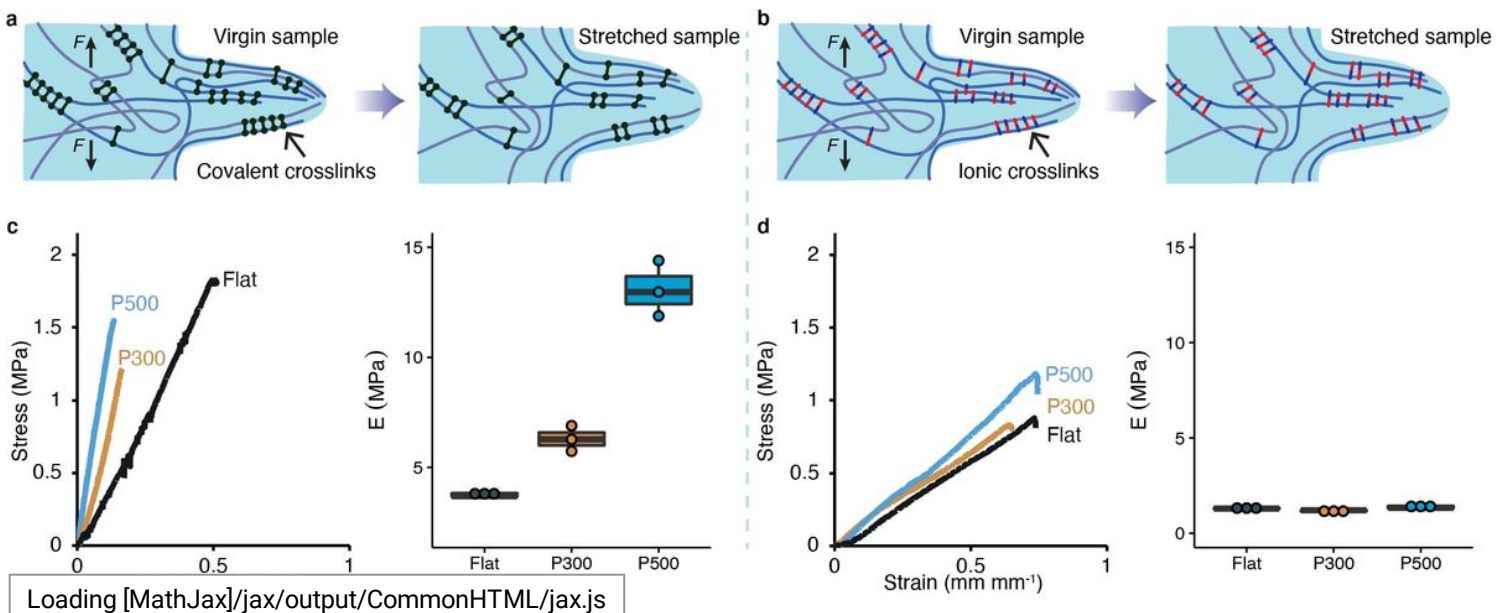


Figure 5

Templating strategy applied to additional biopolymer systems. (a) An illustration of a single chemically crosslinked nanopillar during deformation. The chemical crosslinks serve as rigid bonding sites that rupture during tensile loading. (b) An illustration of a single ionically crosslinked nanopillar during deformation. The dynamic ionic bonds reform during deformation. (c) Typical stress-strain curves of the chemically crosslinked chitosan-genipin films. The Young's modulus, E , of the films increases with the application of the nanopillar surface topography. (d) Typical stress-strain curves of the ionically crosslinked chitosan-TPP films. The Young's modulus, E , of the films is independent of the nanopillar surface topography.

Supplementary Files

This is a list of supplementary files associated with this preprint. Click to download.

- [SupportingInformation.docx](#)
- [SupportingInformation.docx](#)